Article ID: 1006-8775(2021) 02-0177-14

Analysis of Deep Convective Towers in a Southwest-Vortex Rainstorm Event

ZHAI Dan-hua (翟丹华)[1, 2], KONG Fan-you (孔凡铀)[2], DAI Ze-jun (戴泽军)[3], GAO Song (高 松)[4], DENG Cheng-zhi (邓承之)[1], ZHANG Yong (张 勇)[1]

(1. Chongqing Meteorological Observatory, Chongqing 401147 China; 2. Center for Analysis and Prediction of Storms, University of Oklahoma, Norman 73072 USA; 3. Hunan Meteorological Observatory, Changsha 410118 China; 4. Chongqing Institute of Meteorological Sciences, Chongqing 401147 China)

Abstract: The structure and organization of the extreme-rain-producing deep convection towers and their roles in the formation of a southwest vortex (SWV) event are studied using the intensified surface rainfall observations, weather radar data and numerical simulations from a high-resolution convection-allowing model. The deep convection towers occurred prior to the emergence of SWV and throughout its onset and development stages. They largely resemble the vortical hot tower (VHT) commonly seen in typhoons or hurricanes and are thus considered as a special type of VHT (sVHT). Each sVHT presented a vorticity dipole structure, with the upward motion not superpose the positive vorticity. A positive feedback process in the SWV helped the organization of sVHTs, which in turn strengthened the initial disturbance and development of SWV. The meso-γ-scale large-value areas of positive relative vorticity in the mid-to-upper troposphere were largely induced by the diabatic heating and tilting. The strong mid-level convergence was attributed to the mid-level vortex enhancement. The low-level vortex intensification was mainly due to low-level convergence and the stretching of upward flow. The meso-α-scale large-value areas of positive relative vorticity in the low-level could expand up to about 400 hPa, and gradually weakened with time and height due to the decaying low-level convergence and vertical stretching in the matured SWV. As the SWV matured, two secondary circulations were formed, with a weaker mean radial inflow than the outflow and elevated to 300−400 hPa.

Key words: southwest vortex, deep convective towers, diabatic heating, secondary circulations, heavy rain.

CLC number: P444 **Document code:** A

https://doi.org/10.46267/j.1006-8775.2021.017

1 INTRODUCTION

The southwest vortex (SWV, termed by Chinese meteorologists) is a meso - α - scale vortex with a horizontal scale of 300−500 km, mostly notable between 700 and 850 hPa. It often appears under the interaction between the Tibetan Plateau and the special atmospheric circulation in southwest China. The SWV is one of the major rainfall-producing weather systems in China during warm seasons [1, 2], and it is only second to typhoon in terms of intensity, frequency, and area of heavy rainfall. Many flood disasters with serious damages in China are closely related to the SWV [3-6]. For example, in the summer of 1998, the Yangtze River Basin was hit by the worst basin-wide flood event since 1954, which was largely due to the frequent occurrence and eastward propagation of the SWVs [7]. As a source region of the SWV, the Sichuan Basin (SCB) is one of the regions mostly affected by the SWVs [8-13]. For instance, from June 29 to 30, 2013, the SCB suffered from a severe heavy rainfall event because of the SWV. This SWV-associated heavy-rainfall event exhibited a nearly south-north oriented rain band, with the peak amount of 246.9 mm (Fig. 1). The main rain band was located over the upstream of Qiongjiang River Basin, and moved eastward from 0800 BST on June 30 to 0800 BST on July 1, 2013. The propagation direction of the torrential rain band was consistent with the Qiongjiang River flow. The water level at Tai'an hydrological station, located at the downstream of the Qiongjiang River Basin, rose to 253.07 m and reached the record peak at 2114 BST on July 1 [6]. Sun et al. [14] studied this extreme rainfall event, and they mainly focused on the coupling interactions between the plateau vortex and the SWV, and the role of jet streams.

Many studies on SWVs focused on their structural characteristics, formation and maintenance mechanisms, and the eastward propagation mechanisms [15-19]. The interaction of the background flow and the Tibetan Plateau was believed to play an important role in the

Received 2020-11-27 **Revised** 2021-02-15 **Accepted** 2021-05-15

Founding: Operational Technology Research Team Project of Chongqing Meteorological Service (YWGGTD-201702); Technology Innovation and Application Development Key Project of Chongqing (cstc2019jscx-tjsbX0007); Natural Science Foundation of Chongqing (cstc2018jcyjAX0434)

Biography: ZHAI Dan-hua, Senior Engineer, primarily undertaking research on weather forecast and numerical simulation.

Corresponding author: ZHAI Dan-hua, e-mail: i_danhua@163.com

formation of the SWVs [20], and the low-level jet was believed to be a main factor for the formation and development of the SWV [21-22]. Zou and Chen [23] pointed out that the dynamic force of unbalance fields at the top of the planetary boundary layer (PBL) and the positive vorticity advection at 500 hPa are among the key factors affecting the formation and development of SWVs. Moreover, the latent heat release, associated with the cumulus convection, is another factor greatly affecting the development of the SWV [24,17-18].

In recent years, an increasing number of research on SWVs has benefited from the dense observational data and high-resolution numerical simulations. Chen et al. [25] used the mosaic data from the Severe Weather Automatic Nowcast System (SWAN), an operational weather data platform developed by the China Meteorological Administration, to analyze the SWV-associated extremely heavy rainfall occurring in the east of the SCB. They found that there were many meso-β-scale and meso-γ-scale convective systems within the radar echo of the SWV. Liu et al. [26] and Deng et al. [27] analyzed the local circulation patterns and the evolution features of mesoscale convective systems(MCSs) during the torrential rain event caused by the SWV, by using Doppler weather radar 4DVar (4-dimensional variation) assimilation technique. They suggested that heavy-rainfall supercells and meso-γ-scale cyclones often appeared in the MCSs developing stage. With radar mosaic reflectivity data, NCEP (National Centers for Environmental Prediction) reanalysis data and TRMM-PR (precipitation radar of Tropical Rainfall Measuring Mission) data, Zhou et al. [28] analyzed the radar echo structure and its evolution in a severe rainfall event caused by the plateau vortex and the SWV. Lu et al. [29] analyzed the evolution characteristics of the SWV by using a mesoscale numerical model. These studies all show large number of mesoscale or small-scale convections before the formation of SWVs. It is similar to the embryonic phase of typhoons or hurricanes where large number of mesoscale and small-scale convection cells form. Gray [30] related such explosive eruption of "extreme convection" with tens of kilometers in scale to the formation of typhoons. Hendricks et al. [31] and Montgomery et al. [32] named such intense deep cumulonimbus convection cores as vortical hot towers (VHTs), and the strong vertical vorticity can reach the tropopause via nearly undiluted ascent. They also found that such VHTs are of great importance in the formation of tropical storms.

Are the characteristics of deep convective towers before the formation of SWVs similar to those of VHTs in the tropical storms? How do the mesoscale and convective-scale systems develop into a SWV from weak or unorganized disturbances? These two questions are not yet well answered. Therefore, in this study, a torrential rainfall event over the SCB in southwest China from the late afternoon on June 29 to the morning on June 30, 2013 Beijing Standard Time (BST =UTC+8h) is examined by using intensified rainfall observations, radar observation, and high-resolution Weather Research and Forecasting Model (WRF) simulations. The main focuses are the evolution of convective activities before the SWV formation and the roles of such deep convective towers in the genesis and evolution of SWVs.

The remainder of this paper is organized as follows. Section 2 presents the analyses of observational data for the case. Section 3 briefly introduces the numerical weather model system and the verification method. The three-dimensional structure of the hot convective towers and their roles in the SWV formation and evolution, the coupling interactions among the mid-level mesoscale vortex, hot convective towers and the SWV are analyzed in Section 4. Section 5 presents the conclusions and discussion.

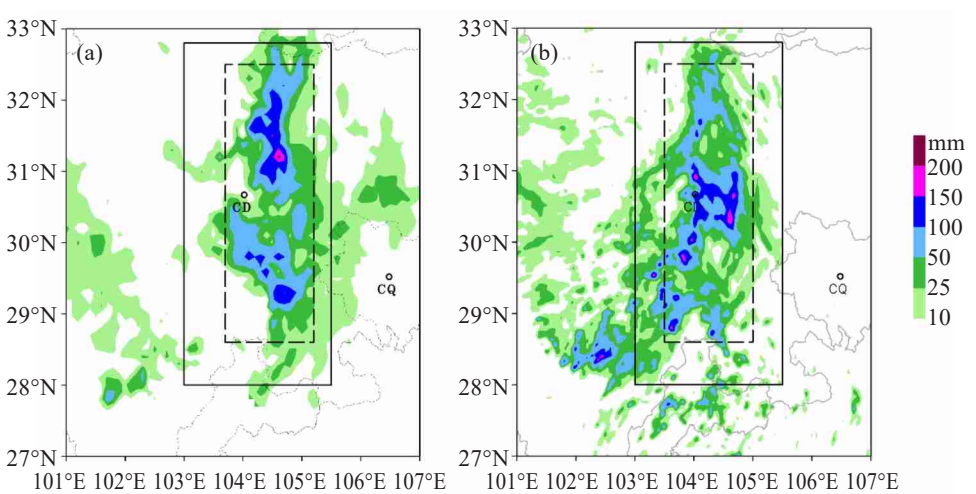

Figure 1. Distribution of the 24-h accumulated surface rain (shaded; units: mm) during the period of 0800 BST 29 Jun-0800 BST 30 Jun 2013 derived from (a) the rain gauges of Sichuan Meteorological Bureau and Chongqing Meteorological Bureau and (b) model simulation from the finest-resolution (3 km) domain.

2 OBSERVATIONAL ANALYSES

The SWV appeared at 700 and 850 hPa at 0800 BST on June 30, 2013 [6, 14]. Fig. 2 shows the large-scale environment of this torrential rainfall event before the formation of the SWV. At 200 hPa the SCB was in the east of the South Asia High, which was favorable for the divergence of upper air. A plateau vortex lied in the northwest of Sichuan Province, and the Western Pacific Subtropical High controlled most of southeast China at 500 hPa, with the SCB in the ascending area between them. The prevailing southwesterly wind at 700hPa over the SCB enhanced from 0800 BST to 2000 BST on June 29, bringing moist air from the Bay of Bengal across the Yunnan-Guizhou Plateau (YGP) into the SCB. The topography forced the southwesterly flow at 850 hPa, with moist air and unstable energy, to shift eastward and northeastward into the SCB. Overall, the synoptic conditions were favorable for the heavy rainfall in the region.

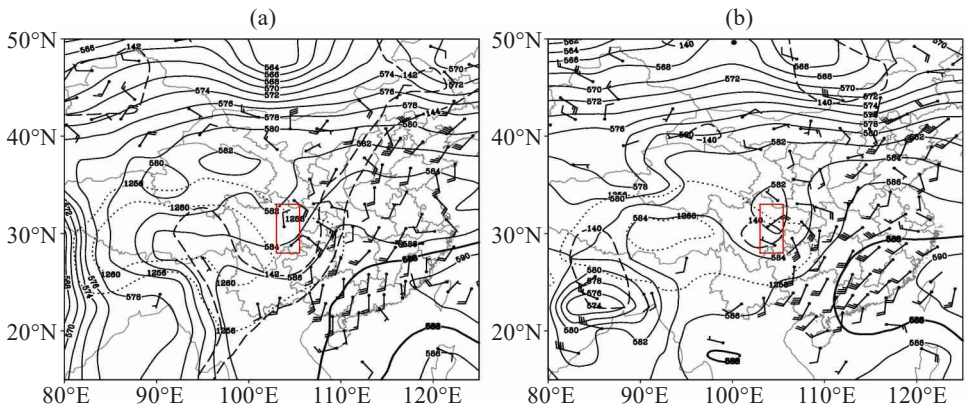

Figure 2. Composite synoptic diagram from soundings at (a): 2000 BST 29 June 2013; (b): 0800 BST 30 June 2013. Geopotential height at 200 hPa (Dotted dashed line, units: dagpm) represents the South Asian High; solid line is geopotential height analyses at 500 hPa (contour interval is 2 dagpm); thick solid line is the 588 dagpm isoline at 500 hPa; barbs are wind fields at 850 hPa (full barb is 4 m s^{-1}, and half-barb is 2 m s^{-1}); long dashed lines are 144, 142 and 140 dapgm isoline at 850 hPa. The MCS concerned is developed within the area marked with the red squared box.

As for the evolution features of the mesoscale and small-scale convective systems during this heavy rainfall event, Fig. 3 shows the time series of radar composite reflectivity derived from the high-resolution 0.01°×0.01° mosaic reflectivity data every 6 minutes from the SWAN system. Deep convective towers with echoes exceeding 35 dBZ began to merge at the northern edge of the Yunnan-Guizhou Plateau at 1318 BST. By 1548 BST, new deep convective towers initiated near the southeast of Chengdu, and both the stratiform echoes on the north and the convective echoes on the south were moving eastward. During 1318−1700 BST, unorganized and scattered deep convective towers were continuously emerging, splitting and merging again. During 1800−2100 BST, the unorganized convective systems started to merge and gradually converge to the center of the severe rainfall. Most of the intensive rainfall occurred from 2100 BST on June 29 to 0400 BST on June 30, when the radar echoes were almost quasi-stationary and highly organized. Shortly after 0400 BST on June 30, the organized MCS began to break into scattered convective clusters around the center of MCS near Chengdu, and dissipated quickly during the morning hours on June 30.

It remains unclear whether the deep convective towers resembled the VHTs found in tropical cyclones when examining the thermomechanics of SWV genesis. More specifically, to what degree are these SWV-associated deep convection towers similar to the tropical storm-associated VHTs, and what roles do they play in the formation of the SWV? To better answer these questions, high-resolution WRF model simulations at convection-allowing grid spacing of 3 km are examined and compared with observations in the next section.

3 NUMERICAL MODEL SIMULATION AND VERIFICATION

The WRF model (version 3.5.1) is used to simulate the deep convective towers and the processes leading to the formation of the SWV. WRF is a community-based nonhydrostatic numerical weather prediction model system with a full set of physics suite ranging from the PBL and land surface process, microphysics and radiations to cumulus parameterization. The model domains are triple nested at 27-9-3 km through two-way nesting (Fig. 4). The innermost domain with 3 km grid spacing falls into convection-allowing resolution, feasible for numerical simulation studies on deep convection weather systems. The descriptions of model grid setting and the model physics parameterizations are summarized in Table 1. The simulation is initialized at 0800 BST on June 29, 2013, and integrated for 36h. The model initial and lateral boundary conditions are derived

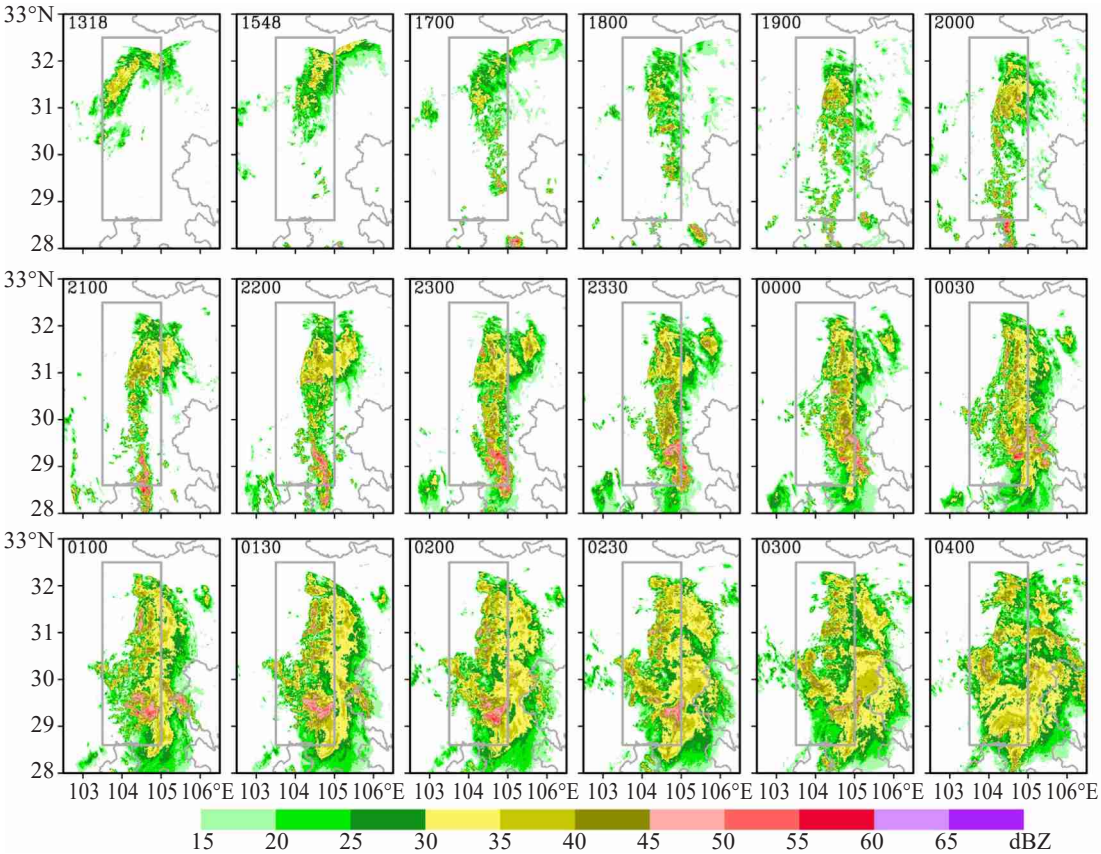

Figure 3. Time series of radar composite reflectivity (units: dBZ) derived from the mosaic reflectivity data using SWAN developed by CMA from 1318 BST 29 June to 0400 BST 30 June.

Table 1. Summary of model configure.

Domain	D01	D02	D03
Grid numbers	200×160	288×216	480×360
Grid resolution	27km	9km	3km
Δvalues (51 levels)	1.00000, 0.99381, 0.98643, 0.97786, 0.96815, 0.95731, 0.94538, 0.93122, 0.91490, 0.89653, 0.87621, 0.85405, 0.82911, 0.80160, 0.77175, 0.73981, 0.70509, 0.66798, 0.62889, 0.58823, 0.54957, 0.51281, 0.47788, 0.44471, 0.41323, 0.38336, 0.35503, 0.32819, 0.30276, 0.27869, 0.25592, 0.23439, 0.21405, 0.19484, 0.17672, 0.15963, 0.14352, 0.12836, 0.11410, 0.10070, 0.08811, 0.07630, 0.06523, 0.05487, 0.04517, 0.03611,0.02765,0.01977,0.01243, 0.00560,0.00000		
Microphysics scheme	Thompson Graupel scheme (2008)		
Longwave radiation scheme	RRTMG scheme (2008)		
Shortwave radiation scheme	RRTMG scheme (2008)		
Planetary boundary layer scheme	MYJ scheme (1994)		
Cumulus parameterization scheme	BMJ scheme (2000)		none
Land surface scheme	Unified Noah land-surface model		

from the 0.5°×0.5° NCEP Global Forecast System final gridded analyses with the outermost lateral boundaries updated every 6 h. The 24-h accumulated rainfall from the WRF simulation in the innermost fine-mesh convection-allowing model domain is compared with the observations (Fig. 1). The simulated rain band is about 20 km to the west of the observation, and the extreme rainfall area is inconsistent with the observation. The model has produced a peak rainfall amount of 196 mm, which is weaker than the observed amount of 246.9 mm.

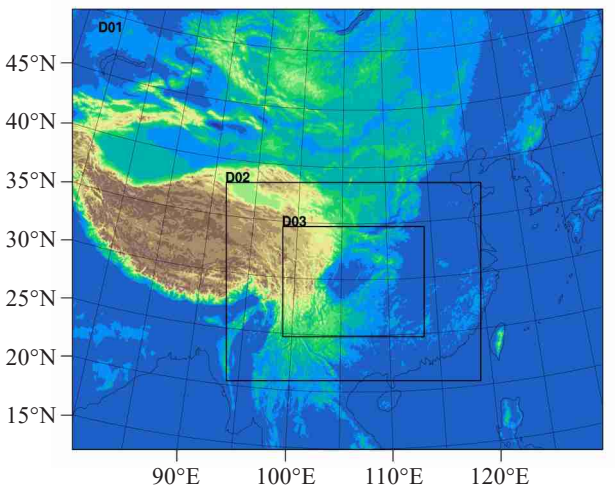

Figure 4. The simulation domains (D01, D02, and D03).

When the large-scale initial conditions with little mesoscale information are taken into consideration, especially over such regions with complex topography, the uncertainties of the model physical schemes and the influence of the Tibetan Plateau on the mesoscale systems could bring difficulties for the model.

To further verify the model performance, Fig. 5 shows the time series of the control-box-averaged hourly rainfall rates between the observation and simulation. The hourly rainfall rates are divided into four intensity levels: heavy (greater than 15 mm h^{-1}), heavy-medium (between 15 and 7 mm h^{-1}), medium (between 7 and 1.5 mm h^{-1}) and light (between 1.5 and 0.1 mm h^{-1}). It is defined according to the hourly rainfall rate classification of the China Meteorological Administration. The observed and simulated rainfall rates are calculated in their respective control boxes (Fig. 1, dashed box). The time series of the total rainfall rate (Fig. 5, top panel) shows the three stages during the storm development. First, it is the growing stage (0800 BST to 2300 BST on June 29), when the hourly rainfall rate gradually increased, especially between 2100 and 2300 BST. The second is the quasi-steady stage (2300 BST on June 29 to 0400 BST on June 30), during which the hourly rainfall rate was almost constant. Third, it is the weakening stage (since 0500 BST on June 30) when the hourly rainfall rate decreased significantly. In the growing stage, the simulated hourly rainfall rate matches

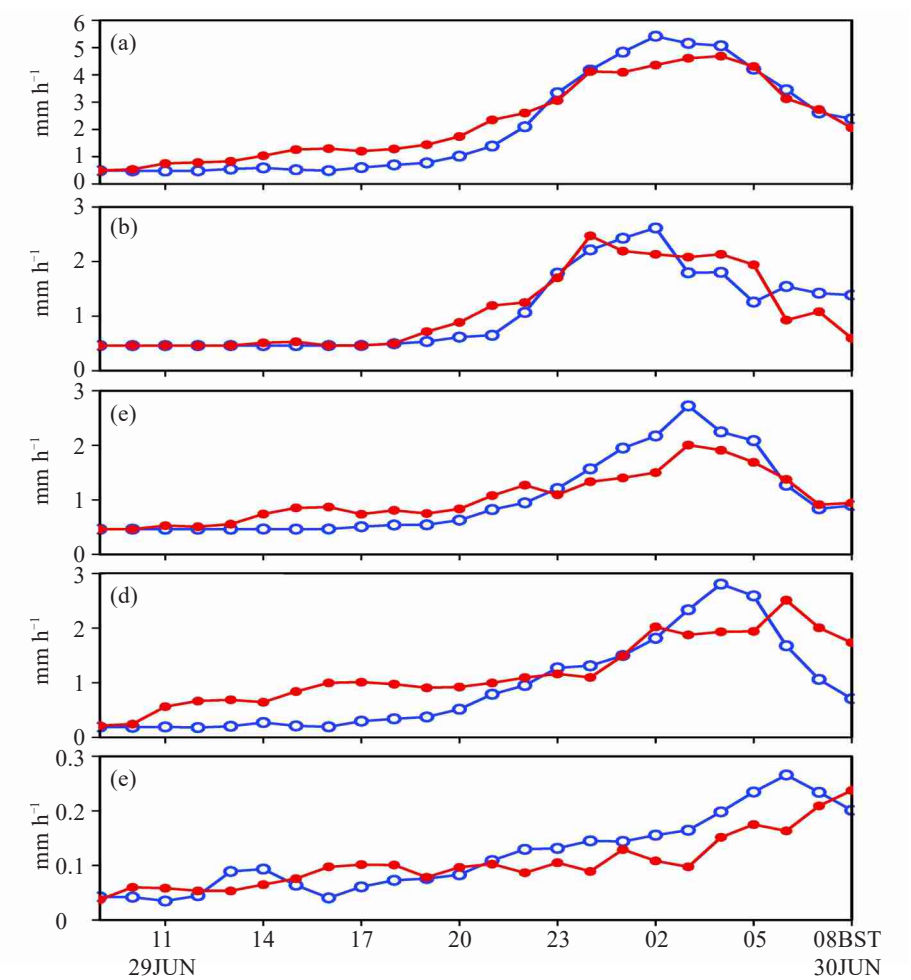

Figure 5. Comparison of the time series of the hourly rainfall rates (units: mm h^{-1}), averaged over the control region, during the period of 0800 BST 29 June-0800 BST 30 June 2013 between the observations (red) and the D03 simulation (blue). (a) the total hourly rainfall rates; (b) the hourly rainfall rates ≥15 mm h^{-1}; (c) 7 mm h^{-1} ≤ the hourly rainfall rates < 15 mm h^{-1}; (d) 1.5 mm h^{-1} ≤ the hourly rainfall rates < 7 mm h^{-1}; (e) the hourly rainfall rates < 1.5 mm h^{-1}.

well with the observation, especially in the heavy rain levels. However, the simulated rainfall is stronger than the observations in total hourly rainfall rate and the two medium rain levels. During the quasi-steady stage, the simulated intensities are a little stronger than the observations except for the heavy classification. The total hourly rainfall rate peaked 2 hours earlier than the observations around 0200 BST on June 30, while the heavy rainfall peaked 2 hours later than the observations. It is suggested that the simulated MCSs strengthened before 0200 BST and weakened after 0200 BST on June 30 more rapidly, and that the model has overestimated the rainfall at the heavy-medium and medium levels during most of the quasi-steady stage.

To further examine the simulated MCSs, the simulated composite reflectivity (Fig. 6) and the radar echo observation (Fig. 3) derived from SWAN are compared. During the growing stage of MCSs in 1300–2100 BST on June 29, the initiation and evolution of deep convective towers on the north edge of YGP matches quite well with the observation. However, the deep convective towers in the middle SCB are weaker, and the numerical model fails to reproduce the stratiform precipitation echoes along the northern SCB. From 2300 BST on June 29 to 0400 BST on June 30, which is the MCSs' merging and organizing stage, the simulated deep convective towers develop more rapidly than the observation before 0200 BST on June 30, and also weaken more rapidly afterwards. As a result, the simulated hourly precipitation rate exceeding 15 mm h^{-1} peaks 2 hours later than the observation, and weakens more rapidly after the peak. Although it is hard to compare the individual convective cell between the simulation and observation, the numerical model still reproduces the general situation of the convective systems. Given the fact that the model simulations can reproduce not only the distribution of the severe rainfall band, but also the main characteristics of the convective systems and their evolution, the simulations from the 27 km and 3 km grids are used to reveal the in-depth features of deep convective towers and their impacts on the formation of the SWV.

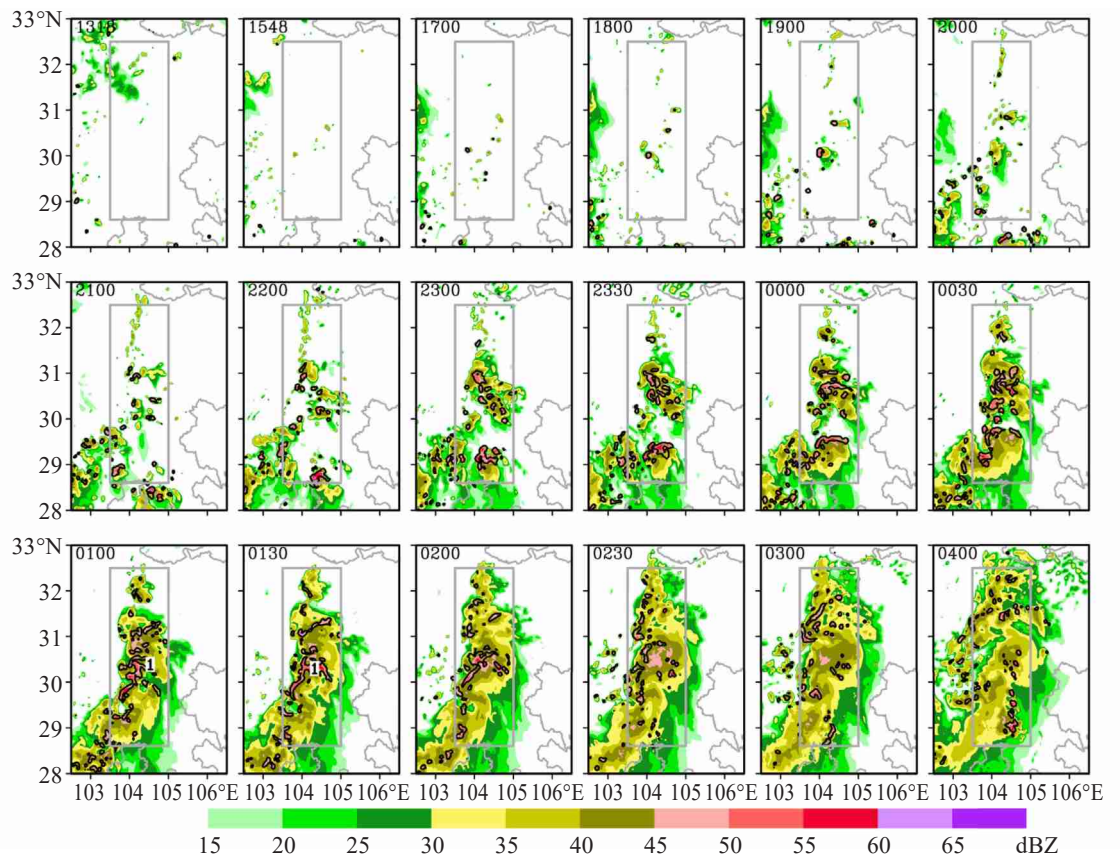

Figure 6. The composite reflectivity (shaded; units: dBZ) and vertical velocity at 500 hPa (value=1m s^{-1}) derived from the simulation with the resolution of 3 km from 1318 BST 29 June to 0400 BST 30 June.

4 RESULTS

4.1 *Comparison between deep convective towers and VHTs in tropical storms*

Aided by the convection-allowing high-resolution numerical simulations, the large number of small-scale deep cumulonimbus convections within the mesoscale convective vortex (MCV) in pre-hurricane environment, with intense cyclonic vorticity in their cores, are referred to as VHT and are deemed as the preferred coherent

structures in hurricane genesis [31-32]. Previous research [31-32,33,35] shows that the typical horizontal scale of the VHTs is about 10−30 km, and the average lifespan is on the order of 1 h. They also have intense upward motion and vorticity. The vertical vorticity in VHTs is attributed to a combination of the MCV tilting of horizontal vorticity, the stretching of MCV and the VHT-generated vertical vorticity. The VHTs are believed to vortically prime the mesoscale environment and collectively mimic quasi-steady diabatic heating rate within the MCV embryo [32]. It would be interesting to examine the degree of the analog of deep convections in this SWV-associated heavy rainfall case to the VHTs in tropical storms.

To investigate the performance of the deep convective towers associated with this SWV case in June, 2013, the WRF output with 3-km grid spacing and 6-min interval is analyzed. Fig. 6 shows that there are many point-like or strip-shaped vertical updraft speed centers within the MCSs. The horizontal scale of the point-like updraft motion is about 10−30 km, while that of the strip-shaped, mainly resulted from the merging of multiple point-like vertical velocity centers, is over 30 km. The area with upward speed exceeding 1 m s^{-1} coincides with that of the deep convective towers with the maximum reflectivity core exceeding 45 dBZ. Most intense upward motions (≥1 m s^{-1}) lasted for no more than 1 h, whereas some towers could last as long as 3 h. The spatio-temporal evolutions of a typical model-simulated maximum instantaneous vertical velocity, diabatic heating rate and maximum reflectivity within a convective cell core are shown in Fig. 7. It is suggested that the vertical velocity greater than or equal to 1 m s^{-1} starts from the PBL and can reach or penetrate the tropopause. The maximum instantaneous vertical velocity occurs at near 250 hPa with the value of about 10 m s^{-1}. According to Montgomery et al. [32], typical VHT cores associated with hurricanes can reach the maximum upward speed of 20−35 m s^{-1} at 9−12 km levels, much more intense than the convection cores in this case. The maximum diabatic heating rate occurs beneath the maximum updraft at about 300 hPa. Thus, the intense upward motions and diabatic heating rates correspond to the strong model-simulated maximum reflectivity.

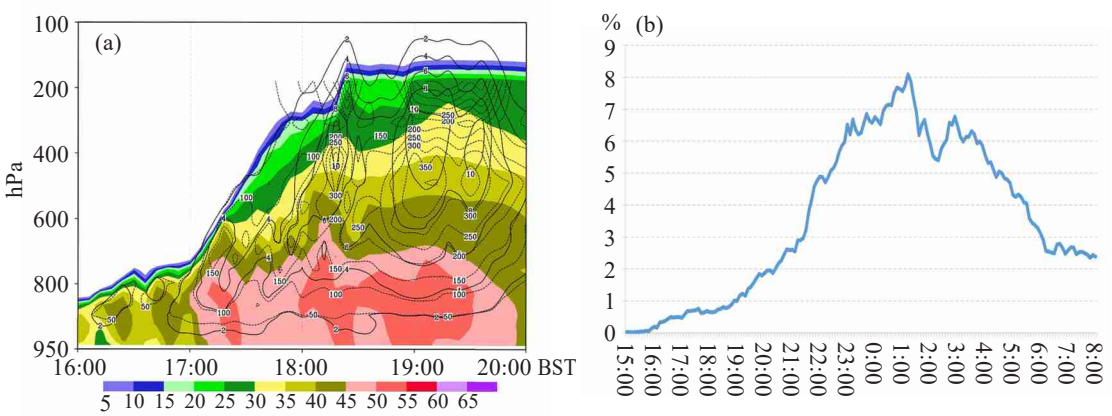

Figure 7. Time-height diagram of maximum instantaneous vertical velocity (black line; units: m s^{-1}), diabatic heating rate (dashed line; units: K h^{-1}), and model-simulated reflectivity (shading; units: dBZ) within the sVHT core (a). Time series of the percentage (units: %) of sVHTs with 600hPa vertical velocity > 1 m s^{-1} in the region (103−105.8°E, 27.4−30.2°N) (b).

To further examine the structures of deep convective towers in this SWV event, Fig. 8 shows the evolution of the relative vertical vorticity and vertical velocity at different times and heights of an individual convective cell. It can be seen that the horizontal scale of the cell is about 15 km from its initiation to maturity at different heights, and the lifespan is less than 2 h after the vertical velocity reaches 1 m s^{-1}. The convective cell also presents a vorticity dipole structure. The upward motion and diabatic heating locate between the positive and negative vorticity centers, and do not superpose the positive vorticity, especially in middle-upper troposphere. This is consistent with the VHTs seen in hurricanes or typhoons [32, 33, 35-36].

Although the magnitude of updrafts in the deep convective towers of this SWV case is weaker than that in hurricanes, the convective behavior, horizontal scale, and lifespan of the deep convective towers are all similar to that of typical VHTs. In order to differentiate them from the VHTs associated with tropical storms, these deep convective towers before the formation of SWV can be viewed as a special type of VHT.

4.2 *Interactions between deep convection towers and mesoscale vortex*

It is found that the initiation and merging of deep convective towers (or sVHTs) are closely related to the development of MCS (Fig. 6 and Fig. 9). The percentage of sVHTs, defined as the areal percentage of vertical velocity greater than 1 m s^{-1} at 600 hPa over the box region between (103−105.8° E, 27.4−30.2° N), peaked at

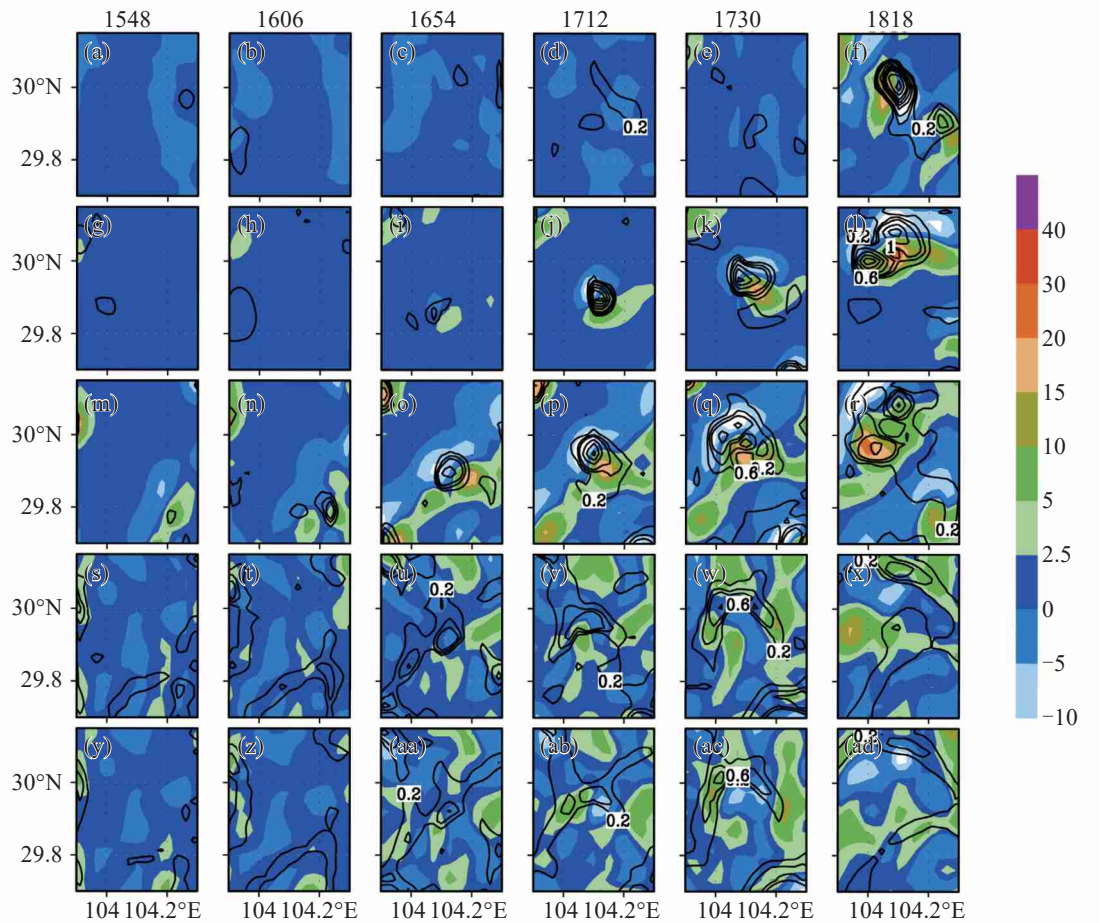

Figure 8. Evolution of the relative vertical vorticity (shaded; units: $10^{-5}s^{-1}$) and vertical velocity (solid line; units: m s^{-1}) at different times and different heights. (a)-(f), (g)-(l), (m)-(r), (s)-(x), (y)-(ad) represent 250 hPa, 500 hPa, 700 hPa, 850 hPa and 900 hPa, respectively. (a), (g), (m), (s), (y) present 1548 BST 29 June; (b), (h), (n), (t), (z) present 1606 BST 29 June; (c), (i), (o), (u), (aa) present 1654 BST 29 June; (d), (j), (p), (v), (ab) present 1712 BST 29 June; (e), (k), (q), (w), (ac) present 1730 BST 29 June; (f), (l), (r), (x), (ad) present 1818 BST 29 June.

0100 BST on June 30, 2013 when the MCS was maturing before the SWV's formation (Fig. 7). In order to understand how the sVHTs and the mesoscale vortex interact, the evolution of wind-stream field and sVHTs is examined in Fig. 9. It is shown that a weak cyclonic circulation appeared at 400 hPa at 1700 BST on June 29 with scattered sVHTs both at 400 hPa (vertical velocity ≥ 1 m s^{-1}) and 850 hPa (relative vorticity ≥ 4×10^{-4} s^{-1}). By 2100 BST, the cyclonic circulation at 400 hPa and sVHTs strengthened, with the latter still scattered. The percentage of sVHTs increased rapidly during this period (Fig. 7). At 2300 BST, the cyclonic circulation center was still at 400hpa, and the horizontal scale was slightly larger at 400 hPa, and a cyclonic disturbance first emerged at 850 hPa. Then it intensified into a SWV at 850 hPa by 0200 BST on June 30. The sVHTs were apparently concentrated toward the circulation center through in the developing stage of SWV. From 0200 BST to 0600 BST on June 30, the coverage areas of SWV further expanded, whereas the sVHTs, mainly located over the east of SWV, were more organized but weakened. The hourly rainfall rate greater than 7 mm h^{-1} (Fig. 5) and the percentage of sVHTs began to decrease from 0100 BST on June 30 (Fig. 7). It is indicated that the middle-level mesoscale vorticity could favor the formation of SWV and the organization of sVHTs. On the other hand, the condensational latent heat associated with sVHTs further strengthened the mesoscale vorticity and promoted the SWV formation, which in turn promoted the merging and organization of sVHTs.

In the previous sections, it is shown that the synoptic environment is favorable for the development and evolution of SWV. Here, the kinematic and thermodynamic structures of the vortex are analyzed to further explore the SWV's development and formation processes, and the features of its secondary circulation. The azimuthal averages of radial wind, tangential wind, vertical wind, and diabatic heating rate are diagnosed based on the innermost model outputs. A mature SWV typically features a closed cyclonic circulation with a diameter about 300−500 km at 700 hPa and/or 850 hPa. A radius of 150 km is thus selected in this study with the system center close to the SWV center. Before the formation of SWV, the center of wind field, with

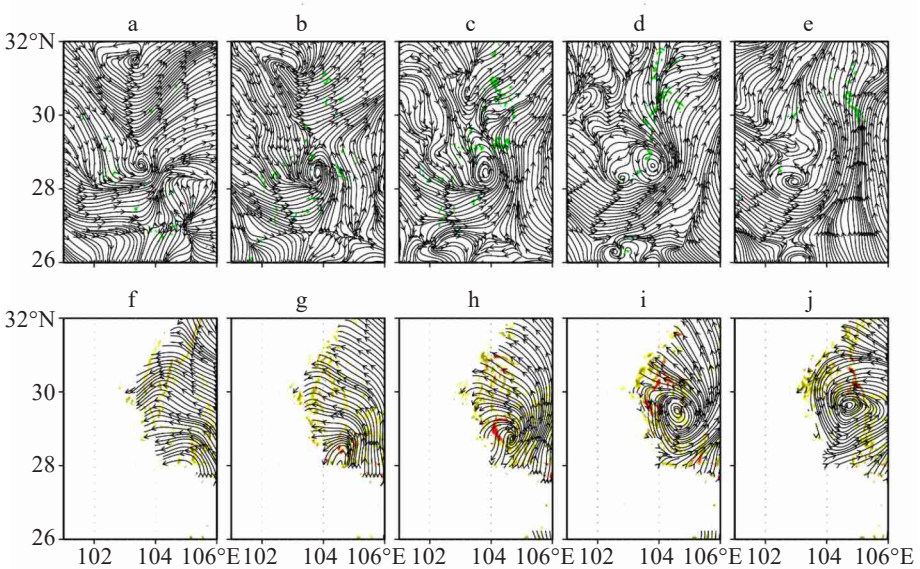

Figure 9. (a)-(e) present wind streamline at 400 hPa and vertical velocity at 600 hPa (shaded, ≥1 m s^{-1}). (f)-(j) present wind streamline and relative vertical vorticity (shaded, ≥ 2*10^{-4} s^{-1}, interval = 2*10^{-4} s^{-1}) at 850 hPa at different times. (a) and (f) are at 1700 BST 29 June; (b) and (g) are at 2100 BST 29 June; (c) and (h) are at 2300 BST 29 June; (d) and (i) are at 0200 BST 30 June; (e) and (j) are at 0600 BST 30 June.

cyclonic rotating tendency at 850 hPa, is approximately viewed as the system center.

Given a variable A, the value of A is firstly transformed from model coordinate system (x, y, δ) to cylindrical coordinate system (x, y, p), and then decomposed into two parts, an azimuthal mean value and a perturbation value following the method of Hendricks et al. [31].

$$A(r,\lambda,p,t) = \bar{A}(r,p,t) + A'(r,\lambda,p,t) \quad (1)$$

where

$$\bar{A}(r,p,t) = \frac{1}{2\pi}\int_0^{2\pi} A \quad (2)$$

Equation (2) is discretized into m azimuthal points at each radius.

$$\bar{A}(r,p,t) = \frac{1}{m}\sum_{j=0}^{m-1} A(r,\lambda_j,p,t) \quad (3)$$

Here, r is the radius from an arbitrary center; p is the geopotential height; λ is the azimuthal angle in radius; t is the time. In this study, because the finest grid spacing is 3 km, the radius increment of 3 km is then selected. Given the radius of the SWV is about 150 km, the number of total azimuthal points m is 50.

Before 2100 BST on June 29, the sVHTs continuously emerged but not well-organized, and there was no sign of disturbance at 850hPa (Fig. 9). This period is regarded as the initialization stage of SWV. In the following five hours from 2100 BST on June 29 to 0200 BST on June 30, numerous emerged sVHTs began to merge and tended to be highly organized, and a closed cyclonic circulation gradually formed at 850 hPa and 700hPa (Fig. 9). This period is regarded as the developing stage of SWV. The mature stage of SWV followed after 0200 BST on June 30 when the closed cyclonic circulation expanded more widely at 850hPa (Fig. 9).

Figure 10 displays the simulated azimuthal-averaged radius-height structures of radial wind, tangential winds, vertical velocity and diabatic heating rate in the initialization stage, when the system center was located at (104.4° E, 28.8° N). It is evident that the mean radial inflow dominated the entire troposphere in 50−100 km range from the center, where obvious convergence occurred due to the intersection of outflow and inflow. In the same region, there was negative mean tangential wind, intense upward motions and positive diabatic heating rate in this region due to the latent heat release associated with the sVHTs. It is consistent with the behavior of convection towers described in Section 4.1. Furthermore, remarkable convergence, negative tangential velocity, intense upward motion and adiabatic heating dominated the region 50-100 km from the center and below 300 hPa. The upper-levels (above 300 hPa) were fully controlled by negative mean tangential wind, with peak value up to − 18 m s^{-1}, probably due to significant divergence caused by the anti-cyclonic circulation in the eastern side of the South Asian High.

During the developing stage of SWV, its center remained at (104.4° E, 28.8° N). Fig. 10 shows that the inflow outside the 50 km radius was throughout the entire troposphere during this period and gradually moved towards the center. It was cut off by the outflow at the mid-levels inside the 50 km radius. At the same time, the mean inflow inside the 50 km radius was intensified, and was lifted to about 300−400 hPa level later and gradually weakened by 0100 BST on June 30 (figure not shown). It was rapidly elevated upwards and developed into a significant positive mean tangential velocity center within 25 km from the center near 850 hPa at 2206 BST on June 29, with the maximum value

exceeding 18 m s^{-1}. Meanwhile, another secondary maximum center was seen near the 25 km radius from the center at 300 hPa, with a magnitude of about 6 m s^{-1}. Remarkable updrafts and condensational latent-heat release were mainly concentrated in the middle and upper levels. On the contrary, the lower troposphere was dominated by weak descending motion and negative diabatic heating rate. Unlike tropical storms with clear warm core in their development stage [31,33,35], this SWV had no warm center in lower and middle levels. Chen et al. [15] also found that an intense and mature SWV possessed a complete deep low without a warm core structure.

During its mature stage of SWV, its center was located at (104.4° E, 28.8° N) (Fig. 10). One significant feature is the formation of a well-defined mean toroidal circulation. A system-wide mean radial inflow developed at middle-upper levels (500−300 hPa), and the outflow was at upper troposphere and mid to low levels (below 500 hPa). Montgomery et al. [32] also revealed the well-defined mean secondary circulation structure in a hurricane case. Zhang and Bao [37] found that in tropical storms, MCVs typically have outflows at the upper and lower troposphere and inflows at the mid troposphere, similar to the characteristics of the SWV during its mature stage in this study. More in-depth examination, however, reveals some key differences between mature SWVs and MCVs. Zhang et al. [40] indicated that typical mid-level MCVs prior to tropical storm genesis have a maximum tangential wind of 5 m s^{-1} in 600−500 hPa level and in 60−80 km radius from the center, whereas a mature SWV has much stronger tangential flow core with maximum magnitude of up to 20 m s^{-1}, and the core is much closer to the vortex center at about 30 km radius and in 500−700 hPa. A typical MCV has outflows inside the boundary layer and near the tropopause in 200−100 hPa, and inflows at mid troposphere. Ascending flows associated with MCVs often occur at 60−80 km radius from the center, with a maximum average updraft speed of 0.3 m s^{-1}, whereas SWVs have much weaker updraft velocities (less than 0.1 m s^{-1}).

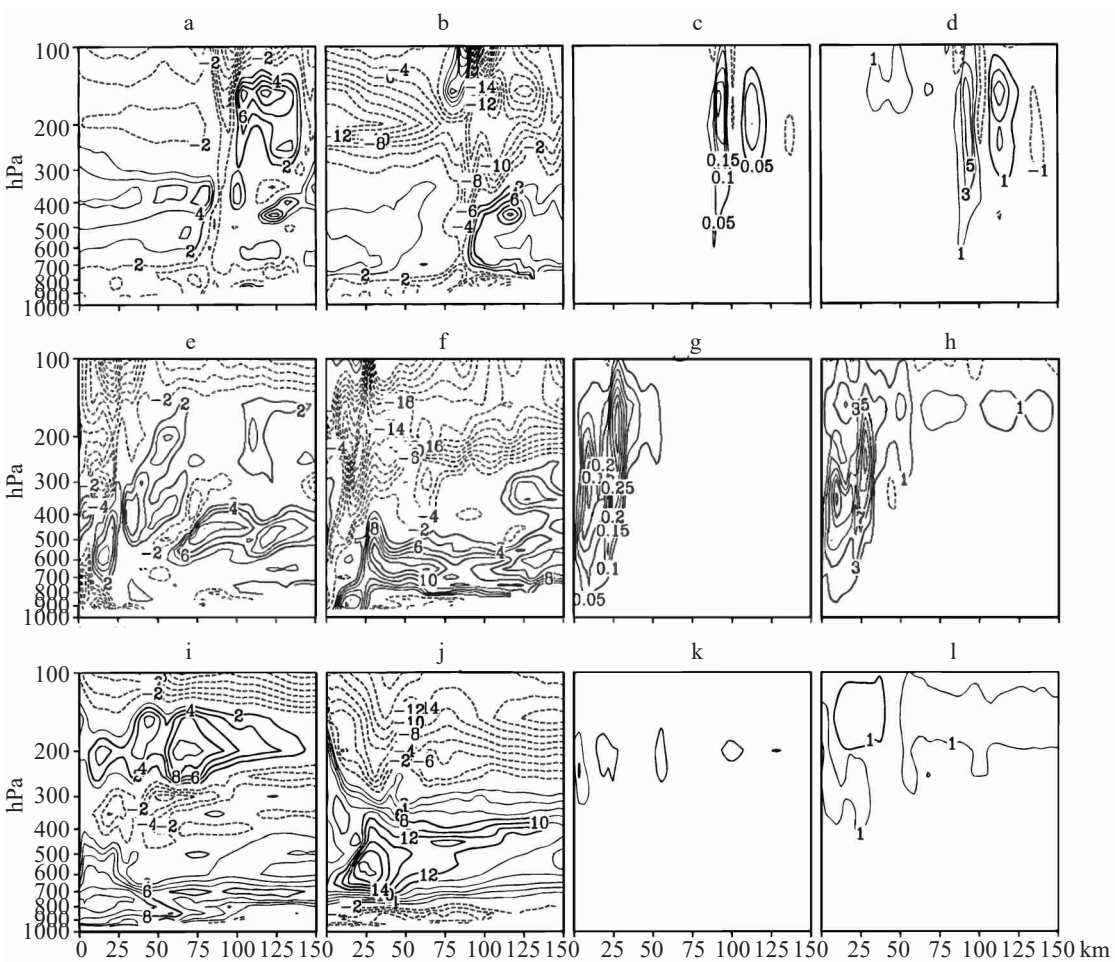

Figure 10. Azimuthal averages of radial wind (units: m s^{-1}) ((a), (e), (i)), tangential wind (units: m s^{-1}) ((b), (f), (j)), vertical velocity (units: m s^{-1}) ((c), (g), (k)) and diabatic heating rate (units: K h^{-1}) ((d), (h), (l)) during different periods. (a)-(d) represents 1900 BST 29 June 2013 (Initial periods), (e)-(h) represents 2206 BST 29 June 2013 (Developing periods), (i)-(l) represents 0630 BST 30 June 2013 (Mature periods). The center is located at (104.4°E, 28.8°N) during initial and developing periods, and is located at (104.4°E, 29.2°N) during mature periods.

4.3 *The roles of sVHTs in the formation of SWV*

To further understand the mechanisms for the vorticity generation during the SWV formation, and in particular the potential contribution of small-scale processes, the scale separation of the vertical-vorticity equation is performed for the model output with 6 min interval. Specifically, the spatial filter based on the two-dimension spectral decomposition of Lin and Zhang [39] is applied to the simulated relative vertical vorticity and divergence fields. The mesoscale processes are first separated into three scales: meso-α-scale (> 250 km) , meso-β-scale (50 ~ 250 km) and meso-γ-scale (< 50 km). The vorticity and divergence with meso-γ-scale are considered to reflect the activity of the sVHTs, while those with meso-α and meso-β scales reflect the activity of the developing SWV. The vertical vorticity equation can be written as:

$$\frac{\mathrm{d}\zeta}{\mathrm{d}t} = -(f+\zeta)\left(\frac{\partial u}{\partial x}+\frac{\partial v}{\partial y}\right) - \left(\frac{\partial w}{\partial x}\frac{\partial v}{\partial z} - \frac{\partial w}{\partial y}\frac{\partial u}{\partial z}\right) + \frac{1}{\rho^2}\left(\frac{\partial \rho}{\partial x}\frac{\partial p}{\partial y} - \frac{\partial \rho}{\partial y}\frac{\partial p}{\partial x}\right) + \frac{\partial F_y}{\partial x} - \frac{\partial F_x}{\partial y} \quad (4)$$

where ζ is the relative vertical vorticity. The terms on the right side of Eq. (4) represent the horizontal convergence of absolute vorticity, tilting, solenoidal effect, and subgrid-scale flux derivatives, respectively. The first two tendency terms of Eq. (4), the horizontal convergence and tilting, are the focus here since the other three terms are two orders of magnitude smaller in values.

Scale separation of the relative vertical vorticity (Fig. 11) shows that the convective clusters (meso-γ-scale vortices) generated strong relative vorticity at middle to upper troposphere (above 400 hPa) from 2000 BST on June 29 to 0200 BST on June 30 (the developing stage of SWV). This is different from typhoons in which the strong relative vorticity region is found mainly at the low levels between 800 and 900 hPa (Lu et al. [29]). There were two meso-α vortices: one at the low levels (800−900 hPa), and the other at mid-levels (600−350 hPa). The low-level vortex occurred prior to the middle-level one. The studies on tropical storms [32, 34, 38] revealed that the low-level system-scale vortex enhancement can ascribe to the vertical stretching effect within VHTs which mainly was confined to the near-surface levels. In this SWV-associated heavy rainfall case, however, the meso-γ-scale vortices were not apparent at the lower troposphere (Fig. 11), so it deserves to understand what are the main factors preventing the formation of low-level vortex.

Figure 12 shows that the stretching term was the most significant near the surface (under 900 hPa) during the developing stage of SWV. According to Eq. 4, the stretching term depends on the absolute vorticity and horizontal divergence. Since the meso-α relative vorticity (Fig. 11, left) was mainly concentrated at the lower troposphere near 800 hPa, the magnitude of meso-γ-scale convergence was weaker than that of meso-α convergence near the surface (Fig. 11, right). The stretching effects near surface are largely ascribed to the system-scale convergence. After 0200 BST on June 30, the low-level vortex gradually weakened due to the negative stretching effects and weak divergence in 900−600 hPa, and gradually extended upward to about 400 hPa.

Figure 7, Fig. 8 and Fig. 11 also show that the sVHTs could generate strong positive relative vorticity at the middle and upper troposphere between 600 hPa and 150 hPa during the developing stage of SWV, when the diabatic heating associated with the ensemble effects of sVHTs is also apparent (Fig. 10). The stretch term, however, is negative (Fig. 12) due to the strong meso-α-scale divergence at upper troposphere (Fig. 11) related to the South Asian High during 2100 BST on June 29 and 0200 BST on June 30. At the same time, the summed negative divergence with horizontal scale smaller than 50 km is greater than −0.6 s^{-1} (Fig. 11), so the effects of meso-γ-scale on the stretch term would be minimal. The tilting term is apparent (Fig. 12) between 300 hPa and 150 hPa during the developing stage of SWV, when the updraft velocity is intense (Fig. 10), so the intense upward motions have contributed to the tilting effect. It is consistent with the center of meso-α-scale convergence located at 300−400 hPa after 0200 BST on June 30, mainly in 0200−0500 BST on June 30 when the stretching and tilting effects were both weak due to weakening meso-γ-scale vorticity and updraft velocity.

5 CONCLUSIONS AND DISCUSSION

In this study, the interaction between an extreme-rain-producing SWV occurred from June 29 to June 30 in the SCB and its associated deep convective towers has been analyzed, by using intensified rainfall observations, radar mosaic composite reflectivity, and the high-resolution convection-allowing WRF simulation output. The structure and organization of the deep convective towers, as well as their roles in the genesis of the SWV are examined.

The WRF simulation with 27-km grid resolution well captured the large-scale features such as the location and life span of the South Asian Subtropical High at 200 hPa, the plateau vortex and the western Pacific subtropical high at 500 hPa. The moisture was transported by the low-level southwesterly airflow from the Bay of Bengal, and the airflow was shifted into the SCB due to the topography of the Daba Mountain below 850 hPa. Still, there are some notable discrepancies between the simulation and the observation. On a positive note, the simulation with the finest-resolution grid at 3 km reproduced quite well the episodes associated with deep convective towers and the genesis time and location of the SWV.

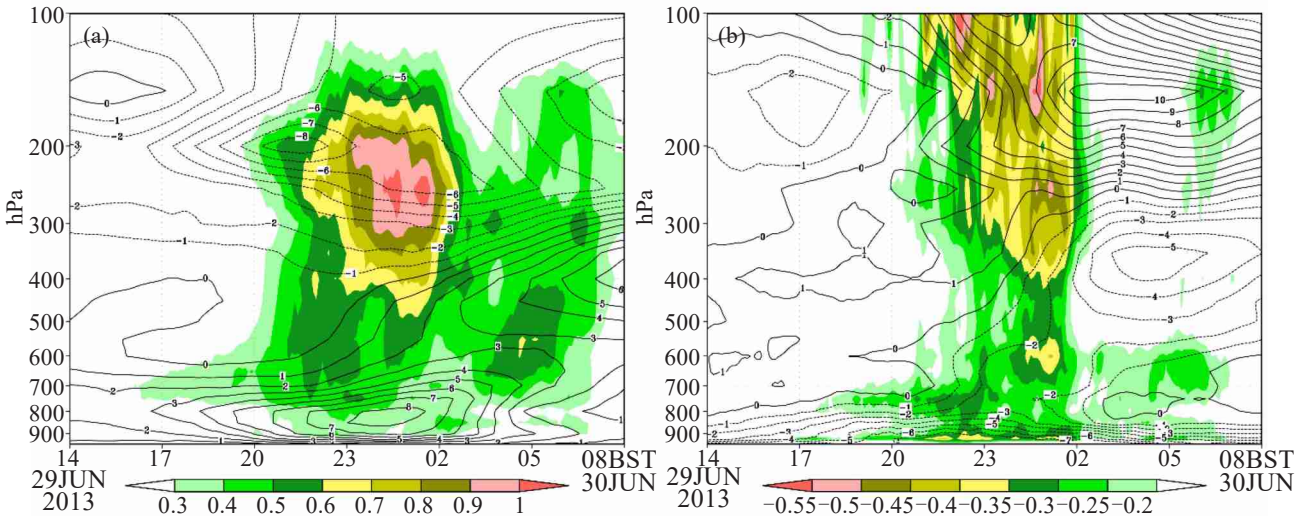

Figure 11. Time-height diagram of the area-average (103−105.8°E, 27.4−30.2°N) absolute vorticity ((a). Contour interval: $1*10^{-5}$ s^{-1}) and divergence ((b). Contour interval: $1*10^{-5}$ s^{-1}) with horizontal scales larger than 250km (meso - α), summed positive relative vorticity (Left one, color shaded, each with $\zeta \geq 5*10^{-4}$ s^{-1}) and summed negative divergence (Right one, color shaded, each with $D \leq 5*10^{-4}$ s^{-1}) with horizontal scales smaller than 50km (meso- γ).

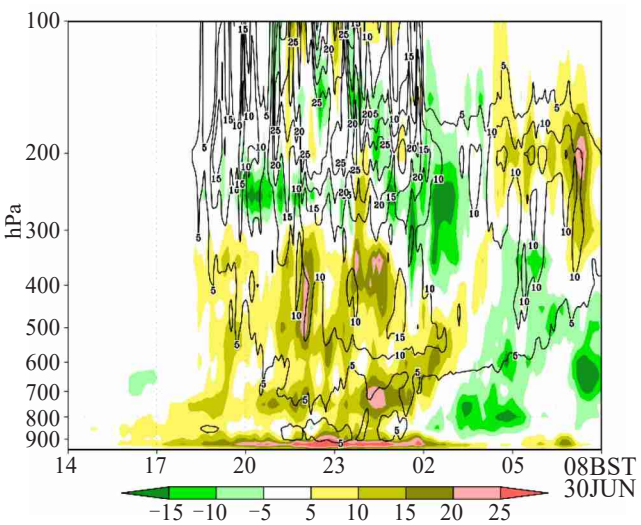

Figure 12. Time-height diagram of the area-average (103−105.8°E, 27.4−30.2°N) stretch term (shaded; units: 10^{-6} s^{-2}) and tilt term (solid line, contour interval; units: $5*10^{-6}$ s^{-2}).

The SWV episode is examined in three distinct stages. During the initial stage, no system-scale toroidal circulation was found. The sVHTs, though still scattered, began to merge. The large-value centers of azimuthally-averaged upward speed and positive diabatic heating rate, both of which were associated with sVHTs, were located 75-km away. During the developing stage of SWV, sVHTs tended to be highly organized. The centers of upward motion and positive diabatic heating, mainly located in mid-to-upper levels, further enhanced and continued moving toward the SWV center. The mean inflow was more remarkable within 25 km radius, the positive tangential velocity core at 850 hPa with the maximum value exceeding 18 m s^{-1}. It is also noteworthy that, different from tropical storms, no warm-center appeared at the middle-low troposphere. The mature stage of the SWV, the averaged upward speed and positive diabatic heating began to weaken rapidly. Two secondary circulations were formed, with the mean radial inflow weaker than the outflow and elevated to 300−400 hPa. The averaged positive tangential velocity was bounded below 300 hPa, with the strongest core located in 700−400 hPa. With these features, the SWV in this case study resembles a typical middle-level MCV illustrated by Wang [24], Zhang [37], and Zhang [38].

The low-level vorticity was mainly caused by meso-α-scale convergence near the surface of weak VHT-type meso - γ - scale vortices. The meso - α - scale positive vorticity reached up to 400 hPa and gradually weakened due to the negative stretching effects and weak divergence in 900−600 hPa during the mature stage of SWV. The sVHTs at middle and upper levels, closely related to the development of the MCS, had large positive relative vorticity induced by upper-level tilting effects and the latent heat release. Such middle-level vortices have the similar structures to MCVs.

Compared with tropical storms like hurricanes or typhoons, the SWV has some remarkably different characteristics. First, the averaged positive tangential velocity in SWVs cannot expand to the entire troposphere as in hurricanes owing to the divergence in the eastside of the South Asian High. Second, SWVs do not have warm-core structure as in typhoons. Furthermore, the latent heating impact under 500 hPa during the mature stage of SWV is weak, as opposite to typhoons in which the latent heating still plays an important role. But the sVHTs in this SWV case

resemble the VHTs associated with typhoons in many aspects. First, both have intense upward motions with an average lifespan of 1 h and feature a vorticity dipole structure. Second, the simulated maximum condensational heating and the maximum vertical velocity are all at upper levels. However, there are also differences between the sVHTs and VHTs, mainly in that the aximum vertical velocity in this SWV is weaker than that in hurricanes or typhoons.

It is worth noting that the meso - α - scale convergence at the middle levels occurred about 3 h before the formation of middle-level positive vorticity, and thus may affect the development and maintaining of SWV. More specifically, the very strong positive vorticity anomalies of the VHTs are always accompanied by strong negative anomalies in their neighborhood. Moreover, the scale separation of divergence shows that the area-averaged value of meso-γ-scale convergence is just slightly larger than that of divergence. Trapp and Weisman [40] and Fang and Zhang [34] discussed the negative relative vorticity anomalies at the low-levels and suggested that such negative anomalies can only remain a few hours before being absorbed by positive anomalies due to the impact of planetary-vorticity convergence. How such negative vorticity and divergence anomalies at the middle and upper levels influence middle-level convergence and vortex should be further investigated. It is also worth noting that tropical storms with clear warm core in their development stage but an intense and mature SWV possessed a complete deep low without a warm core structure, so what is the reason for this difference between these two kinds of vortex systems? And how to coupling interactions between the plateau vortex and the SWV? These questions all need more research.

REFERENCES

[1] TAO S. The Heavy Rainfalls in China [M]. China Science Press, 1980: 255pp (in Chinese).

[2] LU J. The Conspectus of Southwest Vortex [M]. China Meteorological Press, 1986: 275pp (in Chinese).

[3] KUO Y, CHENG L, ANTHE R. Mesoscale analyses of the Sichuan flood catastrophe 11-15 July 1981 [J]. Mon Wea Rev, 1986, 114: 1984-2003, https://doi.org/10.1175/1520-0493(1986)114<1984:MAOTSF>2.0.CO;2.

[4] GAO Z, WANG X, LI W. The statistic characteristics of southwest China vortex and its effect on precipitation of Hubei province [J]. Torrential Rain and Disasters, 2009, 28: 16-26 (in Chinese).

[5] ZHOU H, CUI Y, HU J, et al. Validation of 2008 heavy rain events over the Yangtze River Basin forecast by T639 model [J]. Meteorological Monthly, 2010, 36: 60-67 (in Chinese).

[6] ZHAI D, ZHANG Y, QIU P, et al. Hydrometeorological analysis of two flood events in Qiongjiang river basin [J]. Meteorological Monthly, 2015, 41: 59-67 (in Chinese).

[7] CHEN Z, XU M, MIN W. Relationship between abnormal activities of Southwest vortex and heavy rain the upper reach of Yangtze River during summer of 1998 [J]. Plateau Meteorology, 2003, 22: 162-167 (in Chinese).

[8] ZHAI D, LIU D, LI Q, et al. Feature analysis of Southwest Vortex causing heavy rain in western and middle Chongqing [J]. Plateau Meteorology, 2014, 33(1): 140-147 (in Chinese).

[9] Institute of Plateau Meteorology, China Meteorological Administration and Plateau Meteorological Committee, China Meteorological Society. The 2012's Annals of Southwest Vortex [M]. China Science Press, 2003 (in Chinese).

[10] Institute of Plateau Meteorology, China Meteorological Administration and Plateau Meteorological Committee, China Meteorological Society. The 2013's Annals of Southwest Vortex [M]. China Science Press, 2014 (in Chinese).

[11] Institute of Plateau Meteorology, China Meteorological Administration and Plateau Meteorological Committee, China Meteorological Society. The 2014's Annals of Southwest Vortex [M]. China Science Press, 2015 (in Chinese).

[12] Institute of Plateau Meteorology, China Meteorological Administration and Plateau Meteorological Committee, China Meteorological Society. The 2015's Annals of Southwest Vortex [M]. China Science Press, 2017 (in Chinese).

[13] Institute of Plateau Meteorology, China Meteorological Administration and Plateau Meteorological Committee, China Meteorological Society. The 2016's Annals of Southwest Vortex [M]. China Science Press, 2018 (in Chinese).

[14] SUN J, DENG G, ZHANG Y, et al. Primary study of the extreme rainfall event in Suining City on 30 June 2013 [J]. Meteorological Monthly, 2013, 40: 1174-1182 (in Chinese).

[15] CHEN Z. The dynamic analyses of the effect of large-scale environment flow fields and cumulus on the development of sub-synoptic scale southwest vortex [J]. Plateau Meteorology, 1988, 38: 27-38 (in Chinese).

[16] HE G. Review of the Southwest vortex research [J]. Meteorological Monthly, 2012, 38: 155-163 (in Chinese).

[17] FENG X, LIU C, RASMUSSEN R, et al. A 10-yr Climatology of Tibetan Plateau Vortices with NCEP Climate Forecast System Reanalysis [J]. J Applied Meteorological and Climatology, 2014, 53: 34-46, https://doi.org/10.1175/JAMC-D-13-014.1.

[18] FENG X, LIU C, FAN G, et al. Climatology and structures of southwest vortices in the NCEP climate forecast system reanalysis [J]. J Climate, 2016, 29(21): 7675-7701, https://doi.org/10.1175/JCLI-D-15-0813.1.

[19] ZHONG R, ZHONG L, HUA L, et al. A climatology of the southwest vortex during 1979-2008 [J]. Atmos Oce Sci Lett, 2014, 7(6): 577-583, https://doi. org / 10.3878 / AOSL20140042.

[20] TAO S, DING Y. Observational evidence of the influence of the Qinghai-Xizang (Tibet) Plateau on the occurrence of heavy rain and severe convective storms in China [J]. Bull Amer Meteor Soc, 1981, 62(1): 23-30, https://doi.org/10.1175/1520-0477(1981)062<0023:OEOTIO>2.0.CO;2.

[21] ZHAO Y, WANG Y. A case study on plateau vortex inducing Southwest vortex and producing extremely heavy rain [J]. Plateau Meteorology, 2010, 29: 819-831

(in Chinese).

[22] WANG Z, GAO K, ZHAI G. A mesoscale numerical simulation of low level jet related with the Southwest vortex [J]. Chinese Journal of Atmospheric Sciences, 2003, 27: 75-85 (in Chinese).

[23] ZOU B, CHEN Z. Mesoscale analysis on the formation and development of Southwest vortex during 8-10 July 1989 [J]. Plateau Meteorology, 2000, 19: 141-149 (in Chinese).

[24] WANG W, KUO Y, WARNER T T. A diabatically driven mesoscale vortex in the lee of the Tibetan Plateau [J]. Mon Wea Rev, 1993, 121(9): 2542-2561, https://doi. org / 10.1175/1520-0493(1993)121<2542:ADDMVI>2.0.CO;2.

[25] CHEN G, CHEN Y, ZHANG Y, et al. Causes analysis of the southwest vortex extremely heavy rainfall on 21 July 2012 [J]. Meteor Mon, 2012, 39(12): 1529-1541 (in Chinese).

[26] LIU T, MIAO C, ZHANG Y, et al. Application of doppler radar wind field retrieval technique to southwest vortex rainstorm process [J]. Meteor Mon, 2014, 39(12): 1529-1541 (in Chinese).

[27] DENG C, ZHAO Y, MU R, et al. Evolution features of MCS during a torrential rain caused by southwest vortex [J]. Meteorological Science and Technology, 2018, 46(1): 121-128 (in Chinese).

[28] ZHOU M, LIU L, WANG H. Analysis of the echo structure and its evolution as shown in a severe precipitation event caused by the plateau vortex and the southwest vortex [J]. Acta Meteorologica Sinica, 2014, 72 (3): 554-569 (in Chinese).

[29] LU P, LI Y, ZHENG W, et al. Analysis and numerical simulation of southwest vortex on continuous heavy rain processes in South China [J]. Plateau Meteorology, 2014, 33(6): 1457-1467 (in Chinese).

[30] GRAY W M. The formation of tropical cyclones [J]. Meteor Atmos Phys, 1998, 67: 37-69, https://doi. org / 10.1007/BF01277501.

[31] HENDRICKS E A, MONTGOMERY M T, DAVIS C A. The role of "vortical" hot towers in the formation of Tropical Cyclone Diana (1984) [J]. J Atmos Sci, 2004, 61 (11): 1209-1232, https://doi.org/10.1175/1520-0469(2004) 061<1209:TROVHT>2.0.CO;2.

[32] MONTGOMERY M T, NICHOLLS M E, CRAM T A, et al. A vortical hot tower route to tropical cyclogenesis [J]. J Atmos Sci, 2006, 63(1): 355-386, https://doi. org / 10.1175/JAS3604.1.

[33] ZHANG W, CUI X, WANG A, et al. Numerical simulation of hot towers during pre-genesis stage of typhoon Durian (2001) [J]. J Trop Meteorol, 2008, 32, 619-630 (in Chinese).

[34] FANG J, ZHANG F. Evolution of multi-scale vortices in the development of Hurricane Dolly (2008) [J]. J Atmos Sci, 2011, 68(1): 103-122, https://doi. org / 10.1175 / 2010JAS3522.1.

[35] ZHANG F, SIPPEL J A. Effects of moist convection on hurricane predictability [J]. J Atmos Sci, 2009, 66(7): 1944-1961, https://doi.org/10.1175/2009JAS2824.1.

[36] FUDEYASU H, WANG Y. The multiscale interaction in the life cycle of a tropical cyclone simulated in a global cloud-system-resolving model, Part IIP system-scale and mesoscale processes [J]. Mon Wea Rev, 2010, 138(12): 4305-4327, https://doi.org/10.1175/2010MWR3475.1.

[37] ZHANG D, BAO N. Oceanic cyclogenesis as induced by a mesoscale convective system moving offshore, Part II Parenesis and thermodynamic transformation [J]. Mon Wea Rev, 124(10): 2206-2225, https://doi. org / 10.1175 / 1520-0493(1996)124<2206:OCAIBA>2.0.CO;2.

[38] ZHANG W, CUI X, DONG J. The role of middle tropospheric mesoscale convective vortex in the genesis of typhoon Durian (2001) - Diagnostic analysis of simulated data [J]. Chinese Journal of Atmospheric Sciences, 2010, 34(1): 45-57 (in Chinese).

[39] LIN Y, ZHANG F. Tracing mesoscale gravity waves in baroclinic jet-front systems [J]. J Atmos Sci, 2008, 65(7): 2402-2415, https://doi.org/10.1175/2007JAS2482.1.

[40] TRAPP R J, WEISMAN M L. Low-level mesovortices within squall lines and bow echoes, Part II: their genesis and implications [J]. Mon Wea Rev, 2003, 131(11): 2804-2823, https://doi.org/10.1175/1520-0493(2003)131<2804: LMWSLA>2.0.CO;2.

Citation: ZHAI Dan-hua, KONG Fan-you, DAI Ze-jun, et al. Analysis of deep convective towers in a southwest-vortex rainstorm event [J]. J Trop Meteor, 2021, 27(2): 177-190, https://doi.org/10.46267/j.1006-8775.2021.017.